nature structural & molecular biology

Brief Communication

https://doi.org/10.1038/s41594-023-00951-7

Structural basis for $Ca_V\alpha_2\delta$:gabapentin binding

Received: 5 December 2022

Accepted: 28 February 2023

Published online: 27 March 2023

Check for updates

Zhou Chen[1,6], Abhisek Mondal[1,6] & Daniel L. Minor Jr[1,2,3,4,5]

Gabapentinoid drugs for pain and anxiety act on the $Ca_V\alpha_2\delta$-1 and $Ca_V\alpha_2\delta$-2 subunits of high-voltage-activated calcium channels (Ca_V1s and Ca_V2s). Here we present the cryo-EM structure of the gabapentin-bound brain and cardiac $Ca_V1.2/Ca_V\beta_3/Ca_V\alpha_2\delta$-1 channel. The data reveal a binding pocket in the $Ca_V\alpha_2\delta$-1 dCache1 domain that completely encapsulates gabapentin and define $Ca_V\alpha_2\delta$ isoform sequence variations that explain the gabapentin binding selectivity of $Ca_V\alpha_2\delta$-1 and $Ca_V\alpha_2\delta$-2.

Gabapentin (GBP) (1-(aminomethyl)cyclohexane acetic acid; Neurontin)[1] and the related gabapentinoid drugs pregabalin (Lyrica)[2,3] and mirogabalin (Tarlige)[4,5] are widely used to treat post-herpetic neuralgia, diabetic neuropathy, fibromyalgia, epilepsy, restless leg syndrome and generalized anxiety disorder. These drugs bind to high-voltage-activated calcium channel (Ca_V) $Ca_V\alpha_2\delta$-1 and $Ca_V\alpha_2\delta$-2 subunits[3,4,6–8], but not to the related $Ca_V\alpha_2\delta$-3 and $Ca_V\alpha_2\delta$-4 isoforms[2,9,10]. Gabapentinoid binding to $Ca_V\alpha_2\delta$-1 and $Ca_V\alpha_2\delta$-2 is thought to affect neuronal excitability by impairing Ca_V surface membrane expression[3,7,8] through a mechanism involving Rab11a endosomal recycling[11,12]. Although the GBP-binding site has been identified[13], structural details of $Ca_V\alpha_2\delta$:GBP interactions have not yet been defined.

High-voltage-gated calcium channels (Ca_V1 and Ca_V2)[14,15] are multi-subunit voltage-gated ion channels comprising three key components—the pore-forming $Ca_V\alpha_1$ (refs. 14,15), cytoplasmic $Ca_V\beta$ (ref. 16) and extracellular $Ca_V\alpha_2\delta$ (refs. 1,17) subunits. Recent cryo-EM structural studies of the $Ca_V1.2/Ca_V\beta_3/Ca_V\alpha_2\delta$-1 channel complex[13] revealed a $Ca_V\alpha_2\delta$-1-bound L-leucine, a known $Ca_V\alpha_2\delta$ ligand[1,18,19] and GBP competitor[1,20], that identified the gabapentinoid binding site[1,17]. In this Brief Communication we present the 3.1-Å cryo-EM structure of the $Ca_V1.2/Ca_V\beta_3/Ca_V\alpha_2\delta$-1 channel bound to GBP. The data show that GBP occupies the L-Leu binding site[13] in the first subdomain of the $Ca_V\alpha_2\delta$-1 dCache1 (Ca^{2+} channel and chemotaxis receptor) domain[21]. Structural analysis identifies six binding-site residues that differ between the GBP-sensitive isoforms, $Ca_V\alpha_2\delta$-1 and $Ca_V\alpha_2\delta$-2 (refs. 3,4,6–8), and the GBP-insensitive isoforms, $Ca_V\alpha_2\delta$-3 and $Ca_V\alpha_2\delta$-4 (refs. 2,9,10). These yield steric clashes with GBP and cause binding-site polarity changes that rationalize the GBP-insensitivity of the $Ca_V\alpha_2\delta$-3 and $Ca_V\alpha_2\delta$-4 isoforms.

Structure determination of a recombinant $Ca_V1.2(\Delta C)/Ca_V\beta_3/Ca_V\alpha_2\delta$-1 channel complex[13] comprising a version of human $Ca_V1.2$ truncated after the IQ domain ($Ca_V1.2(\Delta C)$, 186 kDa) having wild-type functional properties[13], rabbit $Ca_V\beta_3$ (54 kDa) and rabbit $Ca_V\alpha_2\delta$-1 (125 kDa) in the presence of 11.7 mM GBP revealed a tripartite channel assembly (~370 kDa) (Fig. 1a) at an overall resolution of 3.1 Å (Extended Data Figs. 1 and 2a–c, and Table 1) largely similar to the L-Leu bound structure[13] (root-mean-square deviation, r.m.s.d.$_{C\alpha}$ = 0.749 Å). As previously observed[13], the sample also contained a chaperone:channel complex of the endoplasmic reticulum (ER) membrane protein complex (EMC)[22–24], $Ca_V1.2(\Delta C)$ and $Ca_V\beta_3$ (Extended Data Figs. 1 and 2d,e). The overall structure of the $Ca_V1.2(\Delta C)/Ca_V\beta_3/Ca_V\alpha_2\delta$-1:GBP complex is similar to other Ca_V1 and Ca_V2 structures[13,25–27]. $Ca_V\alpha_2\delta$-1 has a multi-domain architecture built from two double Cache domains[28], dCache1 and dCache2, and a von Willebrand factor type A (VWA) domain[25,28,29] (Fig. 1a and Extended Data Fig. 3a). Importantly, the high $Ca_V\alpha_2\delta$-1 local resolution (2.0–2.5 Å) and map quality (Fig. 1b–d and Extended Data Figs. 2b,c and 3a–f) allowed detailed comparison of the dCache1 domain with the L-Leu bound structure[13]. A map comparison (Fig. 1b–d and Supplementary Video 1) showed clear differences in the binding pocket density. These included a shape not present in the L-Leu bound maps (Fig. 1b–d) that had features that could be attributed to the GBP cyclohexyl ring and that defined the GBP-binding site.

Similar to L-Leu, GBP occupies a pocket in the first $Ca_V\alpha_2\delta$-1 dCache1 β-barrel lined by Trp207, Val209, Tyr219, Trp225, Tyr238, Arg243, Trp245, Tyr452, Asp454, Ala455, Leu456, Thr463 and Asp493 (Fig. 1e and Extended Data Fig. 3f) that is closed to solvent access. In line with the similar affinities of the two ligands[18], there are no large conformational differences in the dCache1 binding site relative to the

[1]Cardiovascular Research Institute, University of California, San Francisco, CA, USA. [2]Departments of Biochemistry and Biophysics, and Cellular and Molecular Pharmacology, University of California, San Francisco, CA, USA. [3]California Institute for Quantitative Biomedical Research, University of California, San Francisco, CA, USA. [4]Kavli Institute for Fundamental Neuroscience, University of California, San Francisco, CA, USA. [5]Molecular Biophysics and Integrated Bio-imaging Division, Lawrence Berkeley National Laboratory, Berkeley, CA, USA. [6]These authors contributed equally: Zhou Chen, Abhisek Mondal. e-mail: daniel.minor@ucsf.edu

https://doi.org/10.1038/s41594-023-00951-7

$Ca_V\alpha_2\delta$-1:L-Leu complex (r.m.s.d.$_{C\alpha}$ = 0.155 Å; Extended Data Fig. 4a). The structure shows that GBP buries a larger total surface area than L-Leu (409 Å^2 versus 367 Å^2 for GBP and L-Leu, respectively) and that the different sizes and shapes of the ligands alter the details of the hydrogen-bond network surrounding the carboxylate and amino groups found in both ligands (Extended Data Fig. 4b,c). As with the L-Leu complex, Arg243 (Arg217 in some numbering schemes), a key residue for GBP binding to $Ca_V\alpha_2\delta$-1 (ref. 30), is central to the coordination of the GBP carboxylate and makes bidentate interactions to the ligand through its guanidinium group (Fig. 1e and Extended Data Fig. 4b). The importance of this interaction is supported by the observation that an R→A change at this site is known to eliminate GBP binding[3,30], abolish the analgesic effects of GBP and mirogabalin on pain[3,31], and mitigate the effects of pregabalin on seizure and anxiety[32,33]. The Asp493 side chain makes a salt bridge with the GBP amino group that is shorter than the similar interaction in the L-Leu complex (2.7 Å versus 3.2 Å, GBP and Leu, respectively; Fig. 1e and Extended Data Fig. 4b,c). Disruption of this interaction by mutation to alanine strongly reduces the effect of GBP on Ca_V function[28]. Previous studies[30] also showed that two large deletions of 24 and 23 residues (called ΔH and ΔI, respectively[30]) and multiple mutations in these same segments compromise GBP binding. The structure shows that these changes disrupt key $Ca_V\alpha_2\delta$-1 elements that contribute to the integrity of the dCache1 domain (Extended Data Fig. 4d). Together with the previously demonstrated potent effects of R243A[3,30–33] and D493A[28] mutations on gabapentinoid binding and function, the structure underscores the importance of the dCache1 hydrogen-bond network that coordinates the amino and carboxylate moieties shared by amino acid and gabapentinoid $Ca_V\alpha_2\delta$ ligands.

The first subdomain of dCache1 repeats is a common binding site for free amino acids in many archaeal, bacterial and eukaryotic dCache domain containing proteins[28,34], as exemplified by structures of the *Pseudomonas aeruginosa* chemoreceptor PctA[34]. The overall fold of the first $Ca_V\alpha_2\delta$-1 dCache1 domain is largely similar to the amino acid binding the dCache1 domain of bacterial PctA[34] (r.m.s.d.$_{C\alpha}$ = 4.123 Å). However, a structural comparison reveals key differences, including the long $Ca_V\alpha_2\delta$-1 β2-α3 loop, absent from bacterial dCache domains (Extended Data Fig. 4e), the relative position of the β3-β4 loop that covers the ligand-binding pocket, and positional changes in the residues that encircle the ligand (Extended Data Fig. 4f). Nevertheless, $Ca_V\alpha_2\delta$-1 uses the signature dCache1-domain amino acids that recognize the carboxylate (YxxxxRxW) and amino (Y[x_{-27-34}]D) groups of various amino acid-derived ligands in bacterial dCache domains[28] to coordinate the GBP and L-Leu carboxylate (Y238, R243, W245) and amino moieties (Y452, D493) through common hydrogen-bond networks (Extended Data Fig. 4b,c). This network is augmented in $Ca_V\alpha_2\delta$-1 by Ala455, a β3-β4 loop residue (Figs. 1e and 2a) that contributes to carboxylate coordination (Extended Data Fig. 4b,c). In bacterial dCache domains[34], the equivalent of the β3-β4 loop that covers the GBP-binding site moves to open access to the amino acid binding pocket, suggesting that similar $Ca_V\alpha_2\delta$-1 dCache1 motions could provide a means for L-Leu, GBP and other gabapentinoids to access the $Ca_V\alpha_2\delta$-1 binding pocket.

The four different mammalian $Ca_V\alpha_2\delta$ isoforms share a common structure[28], yet GBP and the related gabapentinoids bind to $Ca_V\alpha_2\delta$-1 and $Ca_V\alpha_2\delta$-2 (refs. 3,4,6–8), but not to $Ca_V\alpha_2\delta$-3 and $Ca_V\alpha_2\delta$-4

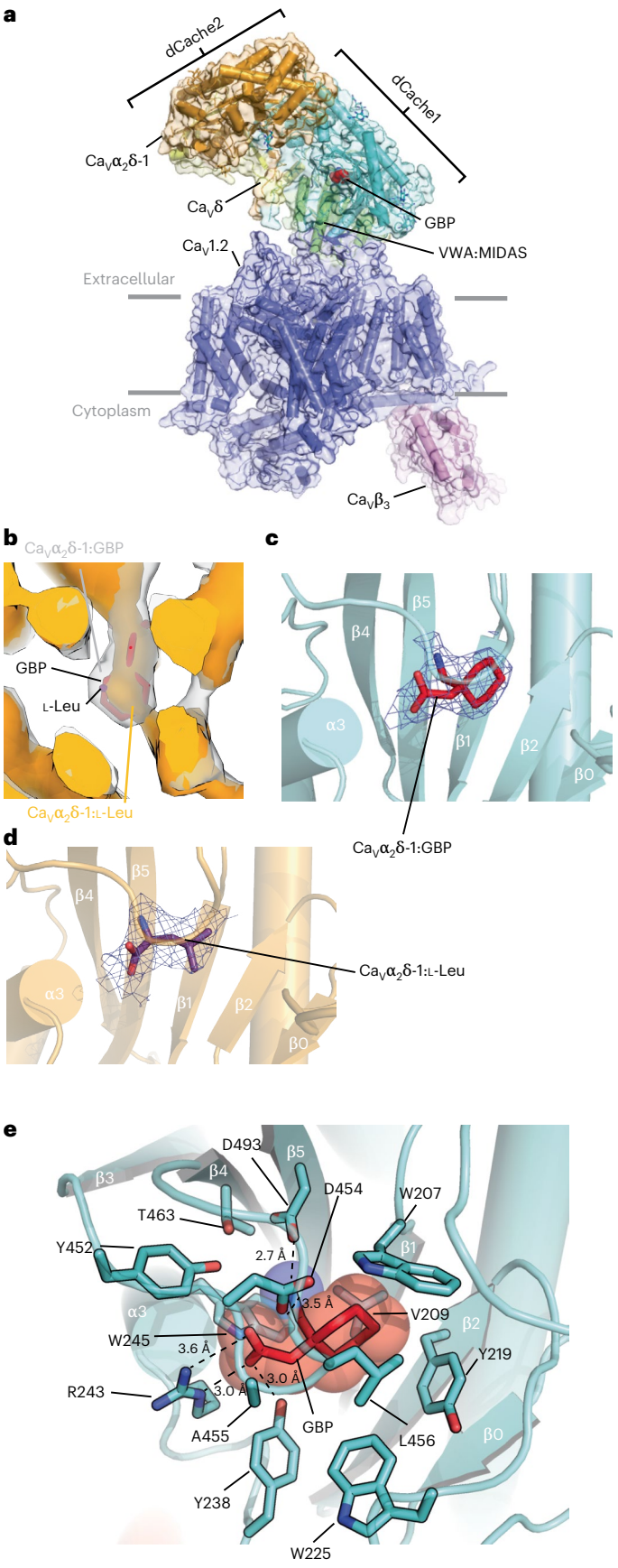

Fig. 1 | Structure of the $Ca_V1.2(\Delta C)/Ca_V\beta_3/Ca_V\alpha_2\delta$-1:GBP complex. a, Side view of the $Ca_V1.2(\Delta C)/Ca_V\beta_3/Ca_V\alpha_2\delta$-1:GBP complex. Subunits are colored with $Ca_V1.2(\Delta C)$ in slate and $Ca_V\beta_3$ in violet. $Ca_V\alpha_2\delta$ domains are colored with dCache1 in aquamarine, dCache2 in orange, VWA:MIDAS in green and $Ca_V\delta$ in yellow. GBP (in red) is shown as space filling. Gray bars denote the membrane. **b**, Comparison of $Ca_V\alpha_2\delta$-1 dCache1 binding sites. Map comparison of the dCache1 ligand-binding site for the GBP complex (clear) and the L-Leu complex[13] (orange). GBP is shown as red sticks. Map label colors match the respective map colors. **c**,**d**, Ligand densities for GBP (10σ, red, **c**) and L-Leu (7σ, violet purple, **d**) in the dCache1 domains are shown as cartoons (aquamarine and light orange, respectively). **e**, $Ca_V\alpha_2\delta$-1 dCache1 ligand-binding site details. GBP (red) and contacting $Ca_V\alpha_2\delta$–1 side chains (green-cyan) are shown as sticks. Distances for the dashed-line interactions are indicated.

https://doi.org/10.1038/s41594-023-00951-7

Table 1 | Statistics for data collection, refinement and validation

	$Ca_V1.2(\Delta C)/Ca_V\beta_3/Ca_V\alpha_2\delta$-1:GBP	
Data collection and processing		
Magnification	105,000	
Voltage (kV)	300	
Electron dose ($e^-/Å^2$)	46	
Defocus range (μm)	−0.9~−1.7	
Pixel size (Å)	0.835	
Symmetry	*C*1	
Initial particle images (no.)	9,703,873	
	$Ca_V1.2(\Delta C)/Ca_V\beta_3/Ca_V\alpha_2\delta$-1:GBP (PDB 8FD7; EMD-29004)	EMC:$Ca_V1.2(\Delta C)/Ca_V\beta_3$ (EMD-29006)
Final particle images (no.)	259,107	383,185
Map resolution (Å)	3.1	3.1
FSC threshold	0.143	0.143
Map resolution range (Å)	~2.4–8.0	~2.4–8.0
Refinement		
Initial model used (PDB code)	8EOG	
Model resolution (Å)	3.3	
FSC threshold	0.5	
Map sharpening *B* factor ($Å^2$)	−20	
Model composition		
Nonhydrogen atoms	19,701	
Protein residues	2,416	
Ligands	20	
B factors ($Å^2$)		
Protein	118.63	
Ligand	42.23	
r.m.s. deviations		
Bond lengths (Å)	0.002	
Bond angles (°)	0.479	
Validation		
MolProbity score	2.16	
Clashscore	7.54	
Rotamer outliers (%)	2.76	
Ramachandran plot		
Favored (%)	93.78	
Allowed (%)	6.10	
Outliers (%)	0.13	

(refs. 2,9,10). Structure-based sequence comparisons identify six sites in the GBP-binding pocket that differ between the gabapentinoid-sensitive ($Ca_V\alpha_2\delta$-1 and $Ca_V\alpha_2\delta$-2[3,4,6–8]) and gabapentinoid-insensitive ($Ca_V\alpha_2\delta$-3 and $Ca_V\alpha_2\delta$-4, refs. 2,9,10) $Ca_V\alpha_2\delta$ isoforms (Fig. 2a). Mapping these on the $Ca_V\alpha_2\delta$-1:GBP structure (Fig. 2b) reveals numerous alterations expected to interfere with GBP binding to $Ca_V\alpha_2\delta$-3 and $Ca_V\alpha_2\delta$-4, including (1) loss of a hydrogen-bond donor to the GBP carboxylate (Y238F), (2) introduction of steric clashes (V209Y, A217F[35] and A455S), two of which (V209Y and A217F) would occupy the same space as the GBP cyclohexyl ring, and (3) changes in contact residue size (Y219I) and polarity (Y219Q, L456Q and A455S) that reshape binding pocket physiochemical characteristics. The $Ca_V\alpha_2\delta$-related protein CACHD1 also lacks most of the key GBP-binding residues (Fig. 2a), indicating that the effects of this protein on Ca_V surface expression[36] are likely to be GBP-independent. Taken together, the multiple changes between the GBP-sensitive and GBP-insensitive isoforms that remove hydrogen bonds, introduce steric clashes and reduce the hydrophobicity of the binding pocket provide a structural rationalization for the differences in gabapentinoid binding properties among the $Ca_V\alpha_2\delta$ isoforms[2–4,7–10].

Binding of GBP and gabapentinoids to the $Ca_V\alpha_2\delta$ subunit of Ca_Vs is critical for the pharmacological effects of this drug class[3,31–33]. The structural identity of the L-Leu[13] and GBP-bound $Ca_V\alpha_2\delta$ complexes (Extended Data Fig. 4a) suggests that the effects of GBP on Ca_V function may arise from changes in the dynamic behavior of $Ca_V\alpha_2\delta$ when it is bound to different ligands. Structural definition of the $Ca_V\alpha_2\delta$ gabapentinoid binding site provides a platform to dissect the mechanisms by which these drugs affect Ca_V function and should guide the

https://doi.org/10.1038/s41594-023-00951-7

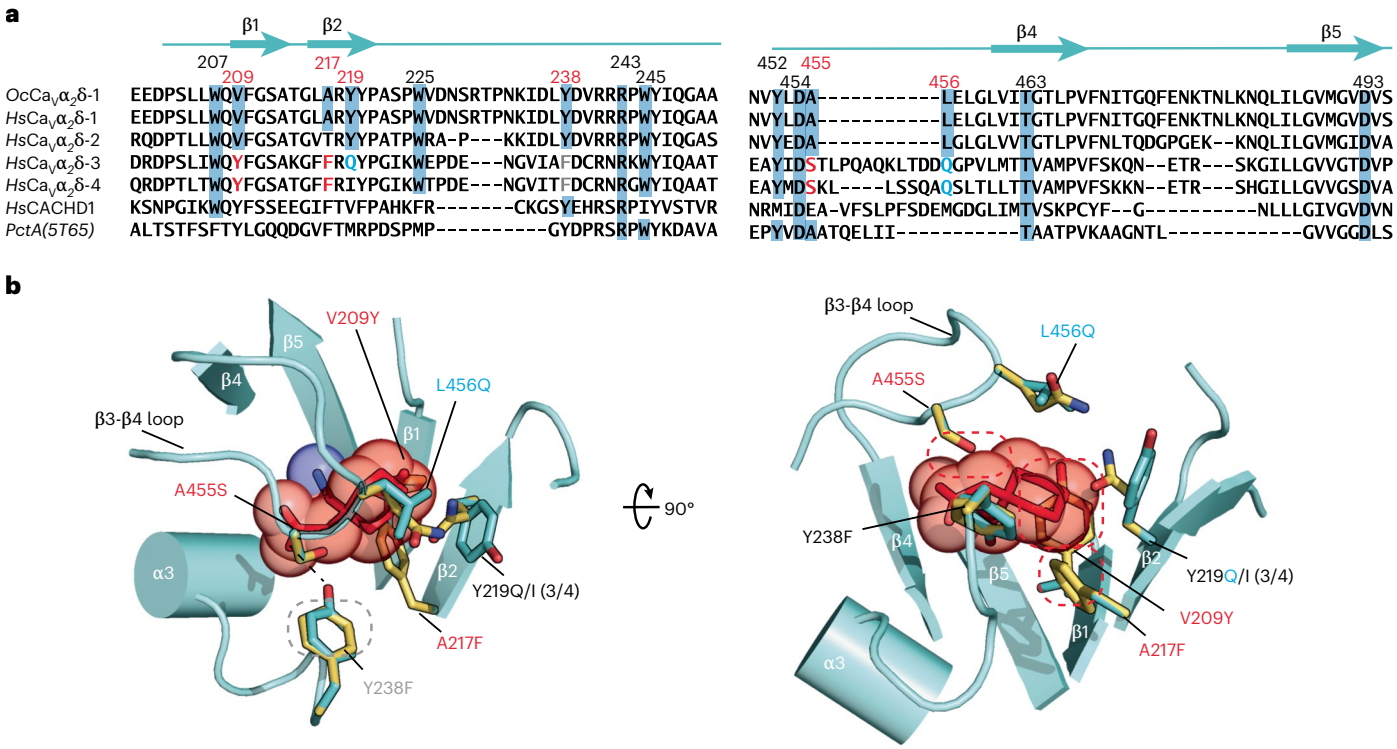

Fig. 2 | Comparison of $Ca_V\alpha_2\delta$-1 GBP-binding sites. a, Sequence comparison of rabbit *Oc*$Ca_V\alpha_2\delta$-1 (NCBI, NP_001075745.1), human *Hs*$Ca_V\alpha_2\delta$-1 (NCBI, NP_001353796.1), *Hs*$Ca_V\alpha_2\delta$-2 (NCBI, NP_006021.2), *Hs*$Ca_V\alpha_2\delta$-3 (NCBI, NP_060868.2), *Hs*$Ca_V\alpha_2\delta$-4 (NCBI, NP_758952.4) and *Hs*CACHD1 (NCBI, NP_065976.3), and bacterial PctA (PDB 5T65)[34] dCache1 domain sequences. Numbers indicate residues interacting with L-Leu and GBP. Red numbers indicate sites that differ between GBP-sensitive and GBP-insensitive isoforms. Residue colors indicate steric clash (red), hydrogen bond loss (gray), and polarity changes (blue) between GBP-sensitive and GBP-insensitive isoforms. **b**, Structural context for amino acid differences between GBP-sensitive (aquamarine) and GBP-insensitive (yellow) $Ca_V\alpha_2\delta$-1 Cache1 ligand-binding sites. GBP-insensitive residues are modeled on the $Ca_V\alpha_2\delta$-1:GBP structure. Dashed ovals denote hydrogen bond loss (gray) and steric clashes (red). (3/4) indicates amino acid changes for $Ca_V\alpha_2\delta$-3 and $Ca_V\alpha_2\delta$-4.

development of next-generation $Ca_V\alpha_2\delta$-directed drugs for the treatment of pain and anxiety.

Online content

Any methods, additional references, Nature Portfolio reporting summaries, source data, extended data, supplementary information, acknowledgements, peer review information; details of author contributions and competing interests; and statements of data and code availability are available at https://doi.org/10.1038/s41594-023-00951-7.

References

1. Dooley, D. J., Taylor, C. P., Donevan, S. & Feltner, D. Ca^{2+} channel $\alpha_2\delta$ ligands: novel modulators of neurotransmission. *Trends Pharmacol. Sci.* **28**, 75–82 (2007).
2. Taylor, C. P., Angelotti, T. & Fauman, E. Pharmacology and mechanism of action of pregabalin: the calcium channel α_2-δ (α_2-δ) subunit as a target for antiepileptic drug discovery. *Epilepsy Res.* **73**, 137–150 (2007).
3. Field, M. J. et al. Identification of the α_2-δ-1 subunit of voltage-dependent calcium channels as a molecular target for pain mediating the analgesic actions of pregabalin. *Proc. Natl Acad. Sci. USA* **103**, 17537–17542 (2006).
4. Domon, Y. et al. Binding characteristics and analgesic effects of Mirogabalin, a novel ligand for the $\alpha_2\delta$ subunit of voltage-gated calcium channels. *J. Pharmacol. Exp. Ther.* **365**, 573–582 (2018).
5. Kato, J., Inoue, T., Yokoyama, M. & Kuroha, M. A review of a new voltage-gated Ca^{2+} channel $\alpha_2\delta$ ligand, mirogabalin, for the treatment of peripheral neuropathic pain. *Expert Opin. Pharmacother.* **22**, 2311–2322 (2021).
6. Gee, N. S. et al. The novel anticonvulsant drug, gabapentin (Neurontin), binds to the $\alpha_2\delta$ subunit of a calcium channel. *J. Biol. Chem.* **271**, 5768–5776 (1996).
7. Bauer, C. S. et al. The increased trafficking of the calcium channel subunit $\alpha_2\delta$-1 to presynaptic terminals in neuropathic pain is inhibited by the $\alpha_2\delta$ ligand pregabalin. *J. Neurosci.* **29**, 4076–4088 (2009).
8. Cassidy, J. S., Ferron, L., Kadurin, I., Pratt, W. S. & Dolphin, A. C. Functional exofacially tagged N-type calcium channels elucidate the interaction with auxiliary $\alpha_2\delta$-1 subunits. *Proc. Natl Acad. Sci. USA* **111**, 8979–8984 (2014).
9. Marais, E., Klugbauer, N. & Hofmann, F. Calcium channel $\alpha_2\delta$ subunits-structure and Gabapentin binding. *Mol. Pharmacol.* **59**, 1243–1248 (2001).
10. Qin, N., Yagel, S., Momplaisir, M. L., Codd, E. E. & D'Andrea, M. R. Molecular cloning and characterization of the human voltage-gated calcium channel $\alpha_2\delta$-4 subunit. *Mol. Pharmacol.* **62**, 485–496 (2002).
11. Meyer, J. O. & Dolphin, A. C. Rab11-dependent recycling of calcium channels is mediated by auxiliary subunit $\alpha_2\delta$-1 but not $\alpha_2\delta$-3. *Sci. Rep.* **11**, 10256 (2021).
12. Tran-Van-Minh, A. & Dolphin, A. C. The $\alpha_2\delta$ ligand gabapentin inhibits the Rab11-dependent recycling of the calcium channel subunit $\alpha_2\delta$-2. *J. Neurosci.* **30**, 12856–12867 (2010).
13. Chen, Z. et al. EMC holdase:Ca_V1.2/$Ca_V\beta$3 complex and Ca_V1.2 channel structures reveal Ca_V assembly and drug binding mechanisms. Preprint at *bioRxiv* https://doi.org/10.1101/2022.10.03.510667 (2022).

14. Zamponi, G. W., Striessnig, J., Koschak, A. & Dolphin, A. C. The physiology, pathology and pharmacology of voltage-gated calcium channels and their future therapeutic potential. *Pharm. Rev.* **67**, 821–870 (2015).
15. Nanou, E. & Catterall, W. A. Calcium channels, synaptic plasticity and neuropsychiatric disease. *Neuron* **98**, 466–481 (2018).
16. Buraei, Z. & Yang, J. The β subunit of voltage-gated Ca^{2+} channels. *Physiol. Rev.* **90**, 1461–1506 (2010).
17. Dolphin, A. C. Voltage-gated calcium channels and their auxiliary subunits: physiology and pathophysiology and pharmacology. *J. Physiol.* **594**, 5369–5390 (2016).
18. Brown, J. P., Dissanayake, V. U., Briggs, A. R., Milic, M. R. & Gee, N. S. Isolation of the [^{3}H]gabapentin-binding protein/$\alpha_2\delta$ Ca^{2+} channel subunit from porcine brain: development of a radioligand binding assay for $\alpha_2\delta$ subunits using [^{3}H]leucine. *Anal. Biochem.* **255**, 236–243 (1998).
19. Dolphin, A. C. Calcium channel auxiliary $\alpha_2\delta$ and β subunits: trafficking and one step beyond. *Nat. Rev. Neurosci.* **13**, 542–555 (2012).
20. David, D. J., Donovan, C. M., Meder, W. P. & Whetzel, S. Z. Preferential action of gabapentin and pregabalin at P/Q-type voltage-sensitive calcium channels: inhibition of K^+-evoked [^{3}H]-norepinephrine release from rat neocortical slices. *Synapse* **45**, 171–190 (2002).
21. Anantharaman, V. & Aravind, L. Cache—a signaling domain common to animal Ca^{2+}-channel subunits and a class of prokaryotic chemotaxis receptors. *Trends Biochem. Sci.* **25**, 535–537 (2000).
22. Jonikas, M. C. et al. Comprehensive characterization of genes required for protein folding in the endoplasmic reticulum. *Science* **323**, 1693–1697 (2009).
23. Christianson, J. C. et al. Defining human ERAD networks through an integrative mapping strategy. *Nat. Cell Biol.* **14**, 93–105 (2011).
24. Hegde, R. S. The function, structure, and origins of the ER membrane protein complex. *Annu. Rev. Biochem.* **91**, 651–678 (2022).
25. Wu, J. et al. Structure of the voltage-gated calcium channel $Ca_v1.1$ at 3.6 Å resolution. *Nature* **537**, 191–196 (2016).
26. Yao, X., Gao, S. & Yan, N. Structural basis for pore blockade of human voltage-gated calcium channel $Ca_v1.3$ by motion sickness drug cinnarizine. *Cell Res.* **32**, 946–948 (2022).
27. Gao, S., Yao, X. & Yan, N. Structure of human $Ca_v2.2$ channel blocked by the painkiller ziconotide. *Nature* **596**, 143–147 (2021).
28. Gumerov, V. M. et al. Amino acid sensor conserved from bacteria to humans. *Proc. Natl Acad. Sci. USA* **119**, e2110415119 (2022).
29. Canti, C. et al. The metal-ion-dependent adhesion site in the von Willebrand factor-A domain of $\alpha_2\delta$ subunits is key to trafficking voltage-gated Ca^{2+} channels. *Proc. Natl Acad. Sci. USA* **102**, 11230–11235 (2005).
30. Wang, M., Offord, J., Oxender, D. L. & Su, T. Z. Structural requirement of the calcium-channel subunit $\alpha_2\delta$ for gabapentin binding. *Biochem. J.* **342**, 313–320 (1999).
31. Oyama, M., Watanabe, S., Iwai, T. & Tanabe, M. Mirogabalin activates the descending noradrenergic system by binding to the $\alpha_2\delta$-1 subunit of voltage-gated Ca^{2+} channels to generate analgesic effects. *J. Pharm. Sci.* **146**, 33–39 (2021).
32. Lotarski, S. et al. Anticonvulsant activity of pregabalin in the maximal electroshock-induced seizure assay in $\alpha_2\delta1$ (R217A) and $\alpha_2\delta2$ (R279A) mouse mutants. *Epilepsy Res.* **108**, 833–842 (2014).
33. Lotarski, S. M. et al. Anxiolytic-like activity of pregabalin in the Vogel conflict test in $\alpha_2\delta$-1 (R217A) and $\alpha_2\delta$-2 (R279A) mouse mutants. *J. Pharmacol. Exp. Ther.* **338**, 615–621 (2011).
34. Gavira, J. A. et al. How bacterial chemoreceptors evolve novel ligand specificities. *mBio* https://doi.org/10.1128/mBio.03066-19 (2020).
35. Page, K. M., Gumerov, V. M., Dahimene, S., Zhulin, I. B. & Dolphin, A. C. The importance of cache domains in $\alpha_2\delta$ proteins and the basis for their gabapentinoid selectivity. *Channels (Austin)* **17**, 2167563 (2023).
36. Dahimene, S. et al. The $\alpha_2\delta$-like protein Cachd1 increases N-type calcium currents and cell surface expression and competes with $\alpha_2\delta$-1. *Cell Rep.* **25**, 1610–1621 (2018).

Methods

Expression and purification of human $Ca_v1.2$

Expression and purification of $Ca_v1.2(\Delta C)/Ca_v\beta_3/Ca_v\alpha_2\delta$-1 was carried out, as previously described[13] using an HEK293S GnTI$^-$ (ATCC #CRL-3022) '$Ca_v\beta_3$-stable' cell line expressing rabbit $Ca_v\beta_3$ (477 residues, UniProt P54286) bearing a Strep-tag II sequence[38]. The codon-optimized construct of human $Ca_v1.2$ bore a C-terminal truncation at residue 1648 (denoted $Ca_v1.2(\Delta C)$), a site located 13 residues after the end of the IQ domain (Δ1649–2138, UniProt Q13936-20, 1,648 residues), followed by a 3C protease cleavage site, monomeric enhanced green fluorescent protein, and a His_8 tag. The second construct carried unmodified rabbit $Ca_v\alpha_2\delta$-1 (1,105 residues, UniProt P13806-1). Both constructs were cloned into modified pFastBac expression vectors having the polyhedrin promoter replaced by a mammalian cell active CMV promoter[39]. All constructs were sequenced completely.

Chemically competent DH10EmBacY (Geneva Biotech) were used to generate the recombinant bacmid DNA, which was then used to transfect *Spodoptera frugiperda* (Sf9; Expression Systems, #94-001F) cells to make baculoviruses for each subunit[40]. $Ca_v1.2$ was expressed in $Ca_v\beta_3$-stable cells together with $Ca_v\alpha_2\delta$-1 using a baculovirus transduction-based system[40]. $Ca_v\beta_3$-stable cells were grown in suspension at 37 °C while supplied with 8% CO_2 in FreeStyle 293 Expression Medium (Gibco) supplemented with 2% fetal bovine serum (Peak Serum), and were transduced with 5% (vol/vol) baculovirus for each target subunit when the cell density reached ~2.5×10^6 cells per ml. Sodium butyrate (10 mM) was added to the cell culture 16–24 h post-transduction, and the cells were subsequently grown at 30 °C. Cells were collected 48 h post-transduction by centrifugation at 5,000*g* for 30 min. The pellet was washed with Dulbecco's phosphate buffered saline (Gibco) and stored at −80 °C.

A cell pellet (from ~3.6 l of culture) was resuspended in 200 ml of resuspension buffer containing 0.3 M sucrose, 1 mM ethylenediaminetetraacetic acid, 10 mM Tris-HCl, pH 8.0 supplemented with 1 mM phenylmethylsulfonyl fluoride, and four Pierce protease inhibitor tablets (Thermo Scientific), then stirred gently on a Variomag magnetic stirrer (Mono Direct, Thermo Scientific) at 4 °C for 30 min. The membrane fraction was collected by centrifugation at 185,500*g* for 1 h and subsequently solubilized in 200 ml of solubilization buffer (buffer S) containing 500 mM NaCl, 5% glycerol (vol/vol), 0.5 mM $CaCl_2$, 20 mM Tris-HCl, pH 8.0, and supplemented with 1% (wt/vol) glycol-diosgenin (GDN) and rotated on an Orbitron rotator II (speed mode S; Boekel Scientific) at 4 °C for 2 h. The supernatant, collected by centrifugation at 185,500*g* for 1 h, was diluted with an equal volume of buffer S to a final concentration of 0.5% GDN and incubated with anti-GFP nanobody Sepharose resin[41] at 4 °C overnight. The resin was loaded on an Econo-Column chromatography column (BioRad) and was then washed stepwise with 20 column volumes (CV) of buffer S supplemented with 0.1% (wt/vol) GDN, 20 CV of buffer S supplemented with 0.02% (wt/vol) GDN, and 20 CV of elution buffer (buffer E) containing 150 mM NaCl, 0.5 mM $CaCl_2$, 0.02% (wt/vol) GDN, 20 mM Tris-HCl pH 8.0. The protein was eluted with 3C protease[42] and subsequently incubated at 4 °C for 2 h with 4 ml of *Strep*-tactin Superflow Plus beads (Qiagen) pre-equilibrated with buffer E. The beads were washed with 20 CV of buffer E, and the protein was eluted with buffer E supplemented with 2.5 mM desthiobiotin. The eluent was concentrated using an Amicon Ultra-15 100-kDa-cutoff centrifugal filter unit (Merck Millipore) before purification on a Superose 6 Increase 10/300 GL gel filtration column (GE Healthcare) pre-equilibrated in buffer E. Concentrated $Ca_v1.2(\Delta C)/Ca_v\beta_3/Ca_v\alpha_2\delta$-1 sample was immediately incubated with GBP (final concentration 2 mg ml^{-1}, 11.7 mM; Sigma-Aldrich) on ice for 4 h before cryo-EM sample preparation, denoted $Ca_v1.2(\Delta C)/Ca_v\beta_3/Ca_v\alpha_2\delta$-1:GBP.

Sample preparation and cryo-EM data acquisition

For cryo-EM, 3.5 µl of 2.0 mg ml^{-1} $Ca_v1.2(\Delta C)/Ca_v\beta_3/Ca_v\alpha_2\delta$-1:GBP was applied to Quantifoil R1.2/1.3 300 mesh Au holey-carbon grids, blotted for 4–6 s at 4 °C and 100% humidity using a FEI Vitrobot Mark IV (Thermo Fisher Scientific), and plunge-frozen in liquid ethane. The cryo-EM grids were screened on an FEI Talos Arctica cryo-TEM system (Thermo Fisher Scientific; at University of California, San Francisco (UCSF) EM Facility) operated at 200 kV and equipped with a K3 direct detector camera (Gatan), and then imaged on a 300-kV FEI Titan Krios microscope (Thermo Fisher Scientific) with a K3 direct detector camera (Gatan; UCSF). Cryo-EM datasets were collected in super-resolution counting mode at a nominal magnification of ×105,000 with a super-resolution pixel size of 0.4175 Å (physical pixel size of 0.835 Å) using a SerialEM v4.1 (ref. 43). Images were recorded with a 2.024-s exposure over 81 frames with a dose rate of 0.57 e^- Å^{-2} per frame. The defocus range was set from −0.9 µm to −1.7 µm.

Image processing and 3D reconstruction

A total of 26,928 movies were collected for $Ca_v1.2(\Delta C)/Ca_v\beta_3/Ca_v\alpha_2\delta$-1:GBP. Initial image processing was carried out in cryoSPARC-3.3[44]. Raw movies were corrected for motion and Fourier binned by a factor of two (final pixel size of 0.834 Å) with the patch motion correction program. Contrast transfer function parameters of the resulting micrographs were estimated with the Patch contrast transfer function estimation program in cryoSPARC-3.3. Particles were picked by blob picking, extracted using a box size of 440 pixel (2× binned to 220 pixels), and 2D-classified using a circular mask diameter of 260 Å. Selected particles represented by good 2D classes were subjected to one round of ab initio reconstruction and heterogeneous refinement with *C*1 symmetry. Particles having reasonable 3D reconstructions (as judged by the Fourier shell correlation (FSC) curve) were re-extracted to physical pixel size and subjected to iterative rounds of ab initio reconstruction and heterogeneous refinement. Further, non-uniform refinements were performed to achieve high-resolution reconstruction.

To improve the $Ca_v\alpha_2\delta$-1 3D reconstruction, multibody refinement was carried out in RELION-3.1[45]. In total, 259,107 refined particles for the $Ca_v1.2(\Delta C)/Ca_v\beta_3/Ca_v\alpha_2\delta$-1:GBP complex were exported from cryoSPARC-3.3 to RELION-3.1 using the csparc2star.py (UCSF pyem v0.5. Zenodo) suite of conversion scripts (https://doi.org/10.5281/zenodo.3576630). Following a 3D refinement in RELION-3.1 using the refined map from cryoSPARC-3.3 and the exported particles, an overall 3.1-Å EM density map (consensus map) was obtained (Extended Data Fig. 1 presents processing flow charts). Multibody refinement was performed in RELION-3.1 to improve the features of the lumenal domain and the transmembrane region for the $Ca_v1.2(\Delta C)/Ca_v\beta_3/Ca_v\alpha_2\delta$-1:GBP complex. We used the phenix.combine_focused_maps program to combine the improved features of the segments from multibody refinement and those of the consensus map to obtain the final map with best features for the $Ca_v1.2(\Delta C)/Ca_v\beta_3/Ca_v\alpha_2\delta$-1:GBP complex[46].

As with an earlier report[13], purification of $Ca_v1.2(\Delta C)/Ca_v\beta_3/Ca_v\alpha_2\delta$-1 yielded a sample that also had a substantial portions of particles (383,185 refined particles) comprising the EMC:$Ca_v1.2(\Delta C)/Ca_v\beta_3$ complex. These refined particles were exported from cryoSPARC-3.3 to RELION-3.1, and subsequent 3D refinement resulted in a 3.1-Å consensus map. Comparison of this 3.1-Å consensus map for the EMC:$Ca_v1.2(\Delta C)/Ca_v\beta_3$ complex with the one reported from the previous study[13] revealed no apparent conformational difference (cross correlation = 0.9554), so the model was not docked for this complex.

Model building and refinement

We used phenix.dock_in_map[46] to dock the $Ca_v1.2(\Delta C)/Ca_v\beta_3/Ca_v\alpha_2\delta$-1 model (PDB 8EOG) into the $Ca_v1.2(\Delta C)/Ca_v\beta_3/Ca_v\alpha_2\delta$-1:GBP map. As the density for $Ca_v\beta_3$ was weaker than for other parts of the channel, we rendered the $Ca_v\beta$ region of the $Ca_v1.2(\Delta C)/Ca_v\beta_3/Ca_v\alpha_2\delta$-1 complex at a threshold of 2.25 (>5 was used for the rest of map) and placed $Ca_v\beta_3$ from the de novo modeled EMC:$Ca_v1.2(\Delta C)/Ca_v\beta_3$ structure (EMD-28376; PDB 8EOI) in the density, followed by rigid-body refinement of the $Ca_v1.2(\Delta C)/Ca_v\beta_3/Ca_v\alpha_2\delta$-1 complex. The docked model and maps were

manually checked and fitted in Coot[47]. Iterative structure refinement and model building were performed using the phenix.real_space_refine program[46]. Restraint files necessary for refinement were generated using phenix.elbow[46,48]. The final statistics of 3D reconstruction and model refinement are provided in Table 1. The per-residue *B* factors, after final refinement against the overall map, were rendered on the refined model and are presented in Extended Data Fig. 2c. The final models were evaluated using MolProbity[49]. All figures and movies were generated using ChimeraX[50] and the Pymol package (v2.4.0; http://www.pymol.org/pymol). Close-contact interaction analyses were performed using LIGPLOT and DIMPLOT[37,51].

Reporting summary

Further information on research design is available in the Nature Portfolio Reporting Summary linked to this Article.

Data availability

$Ca_v1.2(\Delta C)/Ca_v\beta_3/Ca_v\alpha_2\delta$-1:GBP coordinates and maps (PDB 8FD7, EMD-29004, EMD-29007 and EMD-29015) and the map of the EMC:$Ca_v1.2(\Delta C)/Ca_v\beta_3$ complex (EMD-29006) are deposited with the RCSB and EMDB. Requests for materials should be addressed to D.L.M.

References

37. Wallace, A. C., Laskowski, R. A. & Thornton, J. M. LIGPLOT: a program to generate schematic diagrams of protein-ligand interactions. *Protein Eng.* **8**, 127–134 (1995).
38. Schmidt, T. G. & Skerra, A. The Strep-tag system for one-step purification and high-affinity detection or capturing of proteins. *Nat. Protoc.* **2**, 1528–1535 (2007).
39. Liao, M., Cao, E., Julius, D. & Cheng, Y. Structure of the TRPV1 ion channel determined by electron cryo-microscopy. *Nature* **504**, 107–112 (2013).
40. Goehring, A. et al. Screening and large-scale expression of membrane proteins in mammalian cells for structural studies. *Nat. Protoc.* **9**, 2574–2585 (2014).
41. Lee, H., Lolicato, M., Arrigoni, C. & Minor, D. L. Jr Production of K2P2.1 (TREK-1) for structural studies. *Methods Enzymol.* **653**, 151–188 (2021).
42. Shaya, D. et al. Voltage-gated sodium channel (Na_v) protein dissection creates a set of functional pore-only proteins. *Proc. Natl Acad. Sci. USA* **108**, 12313–12318 (2011).
43. Mastronarde, D. N. Automated electron microscope tomography using robust prediction of specimen movements. *J. Struct. Biol.* **152**, 36–51 (2005).
44. Punjani, A., Rubinstein, J. L., Fleet, D. J. & Brubaker, M. A. cryoSPARC: algorithms for rapid unsupervised cryo-EM structure determination. *Nat. Methods* **14**, 290–296 (2017).
45. Zivanov, J. et al. New tools for automated high-resolution cryo-EM structure determination in RELION-3. *eLife* **7**, e42166 (2018).
46. Liebschner, D. et al. Macromolecular structure determination using X-rays, neutrons and electrons: recent developments in Phenix. *Acta Crystallogr. D Struct. Biol.* **75**, 861–877 (2019).
47. Emsley, P., Lohkamp, B., Scott, W. G. & Cowtan, K. Features and development of Coot. *Acta Crystallogr. D* **66**, 486–501 (2010).
48. Moriarty, N. W., Grosse-Kunstleve, R. W. & Adams, P. D. Electronic Ligand Builder and Optimization Workbench (eLBOW): a tool for ligand coordinate and restraint generation. *Acta Crystallogr. D* **65**, 1074–1080 (2009).
49. Williams, C. J. et al. MolProbity: more and better reference data for improved all-atom structure validation. *Protein Sci.* **27**, 293–315 (2018).
50. Pettersen, E. F. et al. UCSF ChimeraX: structure visualization for researchers, educators and developers. *Protein Sci.* **30**, 70–82 (2021).
51. Laskowski, R. A. & Swindells, M. B. LigPlot+: multiple ligand-protein interaction diagrams for drug discovery. *J. Chem. Inf. Model.* **51**, 2778–2786 (2011).

Acknowledgements

We thank D. Bulkley for technical help and K. Brejc for comments on the manuscript. This work was supported by grant no. NIH R01 HL080050 to D.L.M.

Author contributions

Z.C., A.M. and D.L.M. conceived the study and designed the experiments. Z.C. expressed and characterized the samples. Z.C. and A.M. collected and analyzed the cryo-EM data. Z.C. and A.M. built and refined the atomic models. D.L.M. analyzed data and provided guidance and support. Z.C., A.M. and D.L.M. wrote the paper.

Competing interests

The authors declare no competing interests.

Additional information

Extended data is available for this paper at https://doi.org/10.1038/s41594-023-00951-7.

Supplementary information The online version contains supplementary material available at https://doi.org/10.1038/s41594-023-00951-7.

Correspondence and requests for materials should be addressed to Daniel L. Minor.

Peer review information *Nature Structural & Molecular Biology* thanks Rachelle Gaudet and the other, anonymous, reviewer(s) for their contribution to the peer review of this work. Primary Handling Editor: Katarzyna Ciazynska, in collaboration with the *Nature Structural & Molecular Biology* team. Peer reviewer reports are available.

https://doi.org/10.1038/s41594-023-00951-7

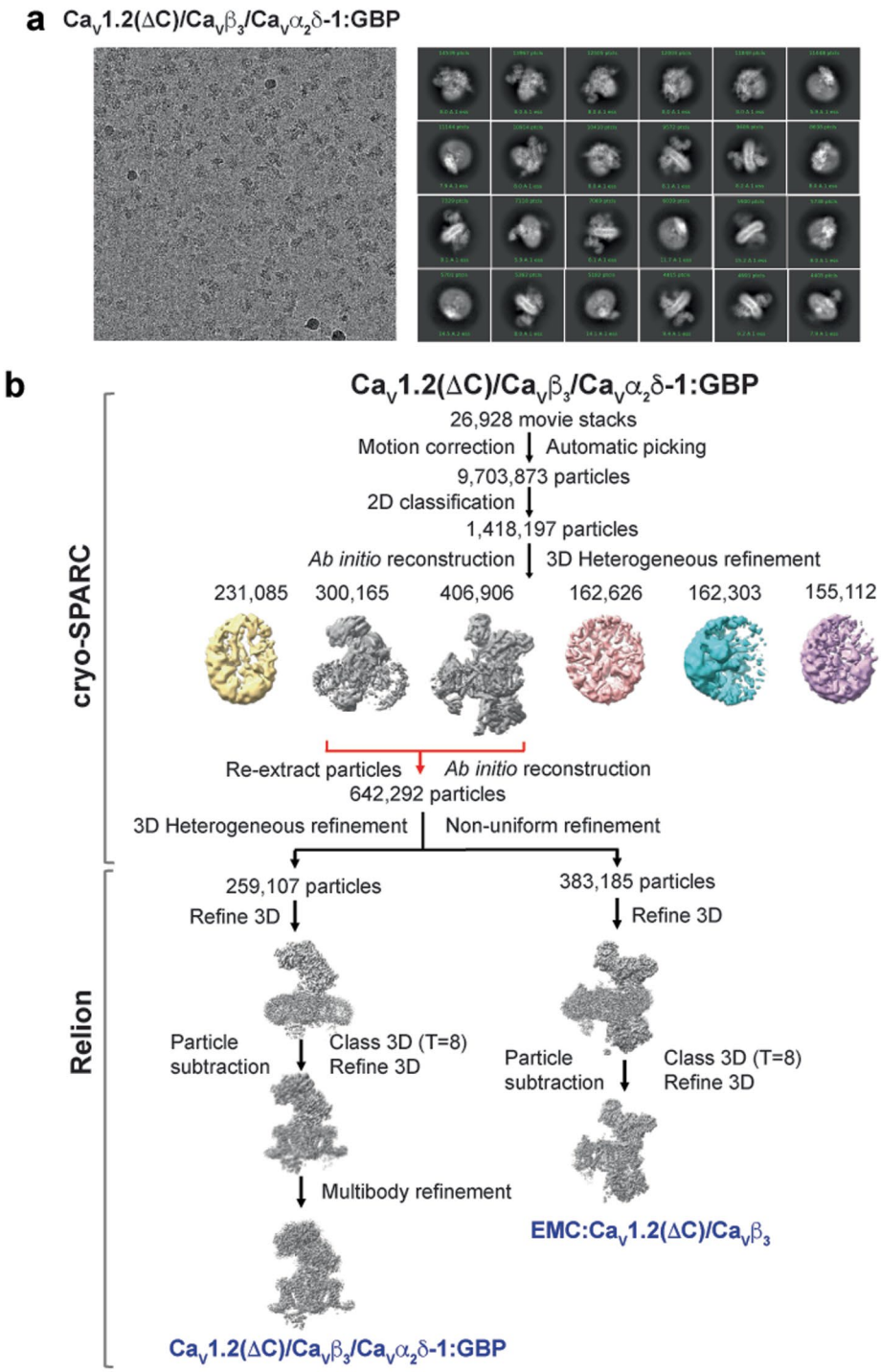

Extended Data Fig. 1 | $Ca_V1.2(\Delta C)/Ca_V\beta_3/Ca_V\alpha_2\delta$-1:GBP Cryo-EM analysis. **a**, Exemplar $Ca_V1.2(\Delta C)/Ca_V\beta_3/Ca_V\alpha_2\delta$-1:GBP electron micrograph (~105,000x magnification) and 2D class averages. N = 3. **b**, Workflow for electron microscopy data processing for $Ca_V1.2(\Delta C)/Ca_V\beta_3/Ca_V\alpha_2\delta$-1:GBP sample. Initial cryoSPARC-3.2 *Ab initio* reconstruction identified a population of particles containing the $Ca_V1.2(\Delta C)/Ca_V\beta_3/Ca_V\alpha_2\delta$-1 and EMC:$Ca_V1.2(\Delta C)/Ca_V\beta_3$ complexes, similar to prior studies[13]. Red arrows indicate the two classes that were re-extracted, subjected to multiple rounds of 3D heterogeneous classification, and exported from cryoSPARC-3.2 for further 3D refinement in RELION-3.1. Particle subtraction was performed for both the refined maps in Relion-3.1 followed by 3D classification with single class and 3D refinement to get the final consensus maps. Multibody refinement was performed to enhance features of $Ca_V\alpha_2\delta$-1, which was used for the $Ca_V1.2(\Delta C)/Ca_V\beta_3/Ca_V\alpha_2\delta$-1:GBP composite map. The composite map was used for model building and refinement.

https://doi.org/10.1038/s41594-023-00951-7

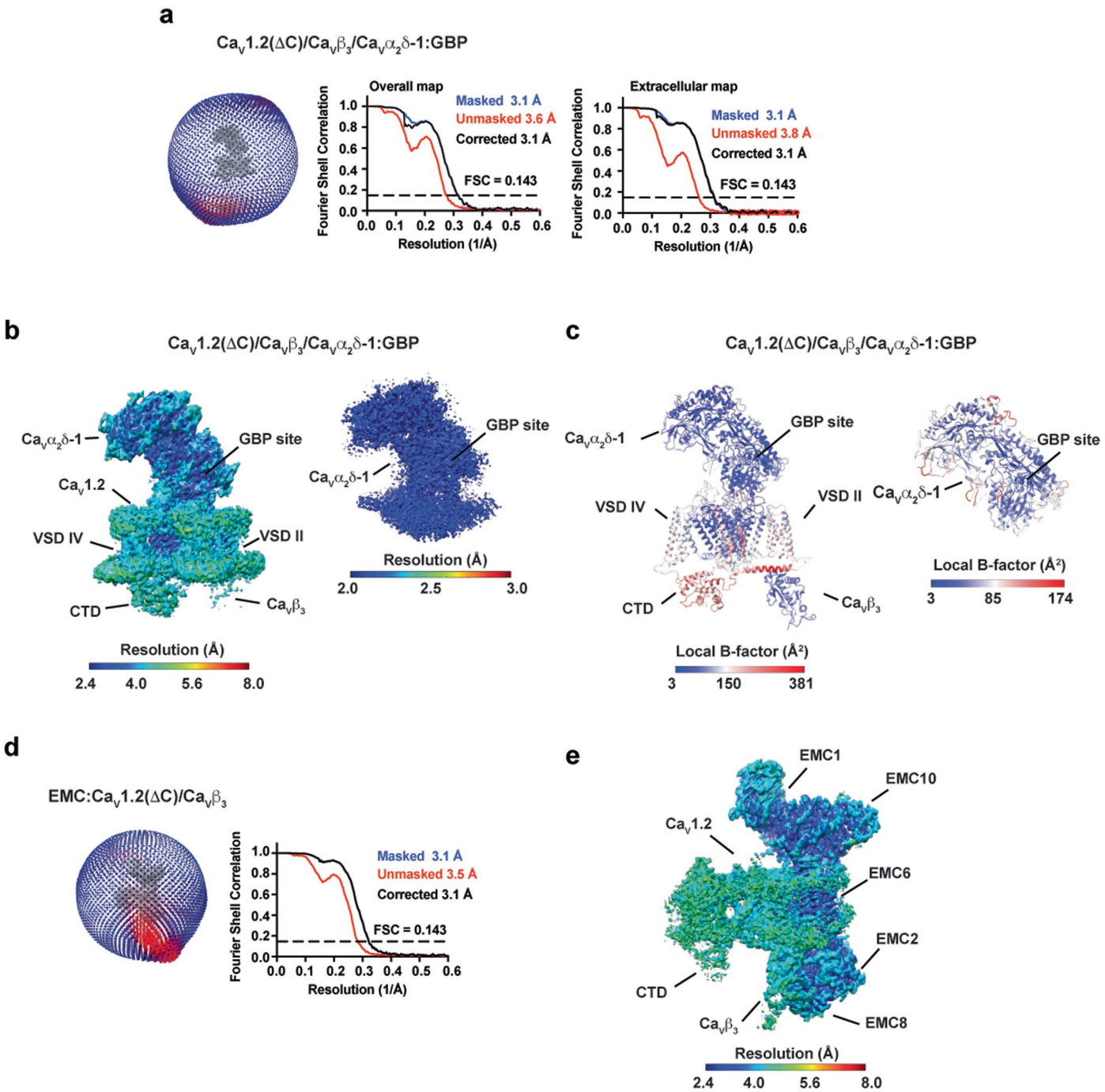

Extended Data Fig. 2 | Ca$_V$1.2(ΔC)/Ca$_V$ β$_3$/Ca$_V$α$_2$δ-1:GBP map and model quality. a, Particle distribution plot and gold-standard Fourier shell correlation (FSC) curve for the overall Ca$_V$1.2(ΔC)/Ca$_V$ β$_3$/Ca$_V$α$_2$δ-1:GBP complex map and the extracellular map containing Ca$_V$α$_2$δ-1:GBP. **b**, local resolution for the overall Ca$_V$1.2(ΔC)/Ca$_V$ β$_3$/Ca$_V$α$_2$δ-1:GBP map and the extracellular map containing Ca$_V$α$_2$δ-1:GBP. **c**, local B-factor for the overall Ca$_V$1.2(ΔC)/Ca$_V$ β$_3$/Ca$_V$α$_2$δ-1:GBP model and the Ca$_V$α$_2$δ-1:GBP subunit. **d**, Particle distribution plot and gold-standard Fourier shell correlation (FSC) curve for the EMC:Ca$_V$1.2(ΔC)/Ca$_V$β$_3$ complex from the Ca$_V$1.2(ΔC)/Ca$_V$ β$_3$/Ca$_V$α$_2$δ-1:GBP sample. **e**, EMC:Ca$_V$1.2(ΔC)/Ca$_V$β$_3$ complex local resolution. Select elements of each complex are labeled.

https://doi.org/10.1038/s41594-023-00951-7

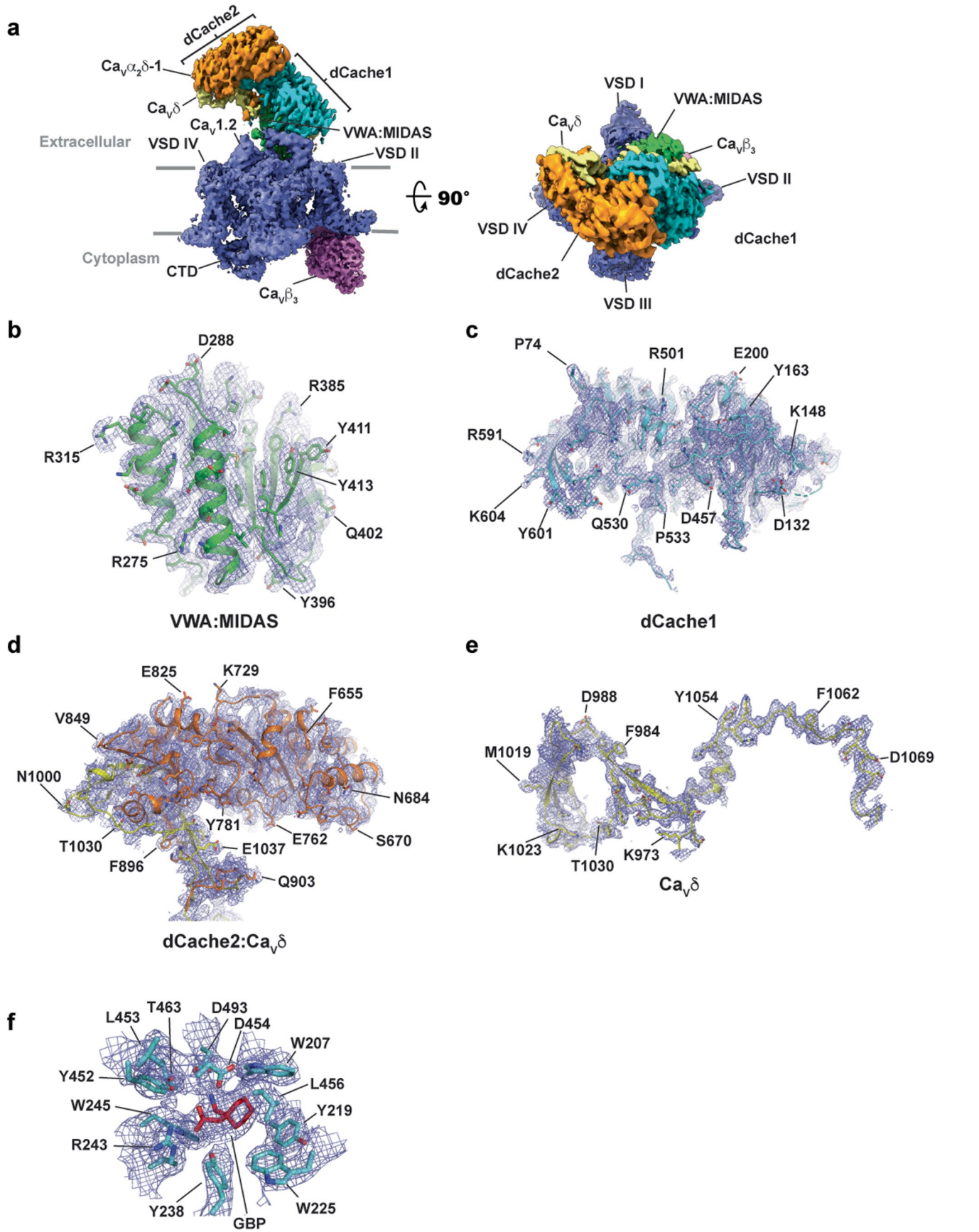

Extended Data Fig. 3 | $Ca_V1.2(\Delta C)/Ca_V\beta_3/Ca_V\alpha_2\delta$-1:GBP Cryo-EM maps. **a**, $Ca_V1.2(\Delta C)/Ca_V\beta_3/Ca_V\alpha_2\delta$-1 side view (left) and extracellular (right) view. Subunits are colored: $Ca_V1.2$ (slate) and $Ca_V\beta_3$ (violet). $Ca_V\alpha_2\delta$ domains are colored as: dCache1 (aquamarine), dCache2 (orange), VWA:MIDAS (green), and $Ca_V\delta$ (yellow). Grey bars denote the membrane. **b**-**e**, $Ca_V\alpha_2\delta$-1 subdomain representative maps for **b**, VWA:MIDAS domain, **c**, dCache1, **d**, dCache2:$Ca_V\delta$. Part of $Ca_V\delta$ completes the second β-barrel subdomain of dCache2, **e**, $Ca_V\delta$. **f**, GBP-binding site. Maps are rendered at 9–10σ. Domain colors are as in **a**.

https://doi.org/10.1038/s41594-023-00951-7

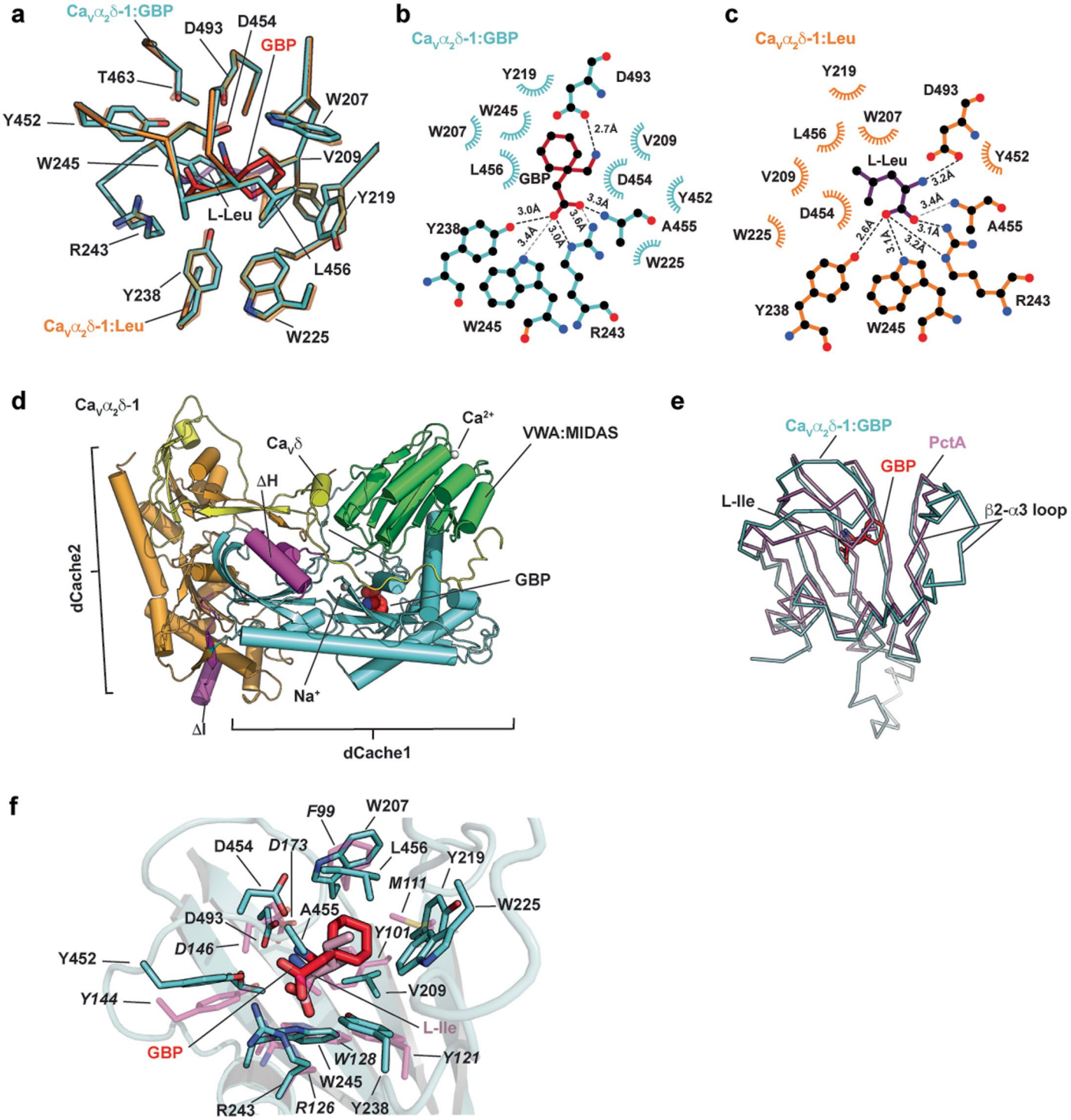

Extended Data Fig. 4 | $Ca_V\alpha_2\delta$-1 GBP-binding site analysis and comparisons. **a**, Superposition of the $Ca_V\alpha_2\delta$-1:GBP (aquamarine) and $Ca_V\alpha_2\delta$-1:L-Leu (orange) (PDB:8EOG)[13] binding sites. GBP is red. L-Leu is purple. **b** and **c**, LigPLOT[37] diagrams of the **b**, $Ca_V\alpha_2\delta$-1:GBP (aquamarine) and **c**, $Ca_V\alpha_2\delta$-1:L-Leu (orange) (PDB:8EOG)[13] binding sites showing hydrogen bonds and ionic interactions (dashed lines) and van der Waals contacts ≤ 5 Å. GBP is red. L-Leu is purple. **d**, Superposition of the first dCache1 repeats from $Ca_V\alpha_2\delta$-1:GBP (aquamarine) and the PctA:L-Ile complex (magenta) (PDB: 5T65)[34]. GBP is red. **e**,**f**, Closeup view of superposition from 'd' showing ligand contact residues. $Ca_V\alpha_2\delta$-1 is shown as a cartoon. GBP is red. Corresponding sidechains of PctA are magenta. L-Ile form the PctA complex is pink. PctA residues are labeled in italics.

nature portfolio

Corresponding author(s): MINOR, Daniel, L., Jr.

Last updated by author(s): Feb 15, 2023

Reporting Summary

Nature Portfolio wishes to improve the reproducibility of the work that we publish. This form provides structure for consistency and transparency in reporting. For further information on Nature Portfolio policies, see our Editorial Policies and the Editorial Policy Checklist.

Statistics

For all statistical analyses, confirm that the following items are present in the figure legend, table legend, main text, or Methods section.

n/a	Confirmed
☒	☐ The exact sample size (*n*) for each experimental group/condition, given as a discrete number and unit of measurement
☐	☒ A statement on whether measurements were taken from distinct samples or whether the same sample was measured repeatedly
☒	☐ The statistical test(s) used AND whether they are one- or two-sided *Only common tests should be described solely by name; describe more complex techniques in the Methods section.*
☒	☐ A description of all covariates tested
☒	☐ A description of any assumptions or corrections, such as tests of normality and adjustment for multiple comparisons
☒	☐ A full description of the statistical parameters including central tendency (e.g. means) or other basic estimates (e.g. regression coefficient) AND variation (e.g. standard deviation) or associated estimates of uncertainty (e.g. confidence intervals)
☒	☐ For null hypothesis testing, the test statistic (e.g. *F*, *t*, *r*) with confidence intervals, effect sizes, degrees of freedom and *P* value noted *Give P values as exact values whenever suitable.*
☒	☐ For Bayesian analysis, information on the choice of priors and Markov chain Monte Carlo settings
☒	☐ For hierarchical and complex designs, identification of the appropriate level for tests and full reporting of outcomes
☒	☐ Estimates of effect sizes (e.g. Cohen's *d*, Pearson's *r*), indicating how they were calculated

Our web collection on statistics for biologists contains articles on many of the points above.

Software and code

Policy information about availability of computer code

Data collection	UCSF SerialEM v4.1, Mastronarde, D. N. Automated electron microscope tomography using robust prediction of specimen movements. J Struct Biol 152, 36-51, doi:10.1016/j.jsb.2005.07.007 (2005).
Data analysis	cryoSPARC-3.2, Punjani, A., Rubinstein, J. L., Fleet, D. J. & Brubaker, M. A. cryoSPARC: algorithms for rapid unsupervised cryo-EM structure determination. Nat Methods 14, 290-296, doi:10.1038/nmeth.4169 (2017). RELION-3.1 Zivanov, J. et al. New tools for automated high-resolution cryo-EM structure determination in RELION-3. Elife 7, doi:10.7554/eLife.42166 (2018). PHENIX, Liebschner, D. et al. Macromolecular structure determination using X-rays, neutrons and electrons: recent developments in Phenix. Acta Crystallogr D Struct Biol 75, 861-877, doi:10.1107/S2059798319011471 (2019). COOT, Emsley, P., Lohkamp, B., Scott, W. G. & Cowtan, K. Features and development of Coot. Acta Crystallogr D Biol Crystallogr 66, 486-501, doi:10.1107/S0907444910007493 (2010). ChimeraX, Pettersen, E. F. et al. UCSF ChimeraX: Structure visualization for researchers, educators, and developers. Protein Sci 30, 70-82, doi:10.1002/pro.3943 (2021). MolProbity, Williams, C. J. et al. MolProbity: More and better reference data for improved all-atom structure validation. Protein Sci 27, 293-315, doi:10.1002/pro.3330 (2018).

PYMOL v2.4.0 http://www.pymol.org/pymol

For manuscripts utilizing custom algorithms or software that are central to the research but not yet described in published literature, software must be made available to editors and reviewers. We strongly encourage code deposition in a community repository (e.g. GitHub). See the Nature Portfolio guidelines for submitting code & software for further information.

Data

Policy information about availability of data

All manuscripts must include a data availability statement. This statement should provide the following information, where applicable:

- Accession codes, unique identifiers, or web links for publicly available datasets
- A description of any restrictions on data availability
- For clinical datasets or third party data, please ensure that the statement adheres to our policy

Cav1.2(ΔC)/Cavbeta3/Cavalpha2∂-1:GBPcoordinates and maps (PDB:8FD7; EMD-29004) and map of the EMC:Cav1.2(ΔC)/Cavbeta3complex (EMD-29006) are deposited with the RCSB.

Human research participants

Policy information about studies involving human research participants and Sex and Gender in Research.

Reporting on sex and gender	n/a
Population characteristics	n/a
Recruitment	n/a
Ethics oversight	n/a

Note that full information on the approval of the study protocol must also be provided in the manuscript.

Field-specific reporting

Please select the one below that is the best fit for your research. If you are not sure, read the appropriate sections before making your selection.

☒ Life sciences ☐ Behavioural & social sciences ☐ Ecological, evolutionary & environmental sciences

For a reference copy of the document with all sections, see nature.com/documents/nr-reporting-summary-flat.pdf

Life sciences study design

All studies must disclose on these points even when the disclosure is negative.

Sample size	Several million particle images were used for the cryo-EM analysis. These particles were classified into different states using reference-free classification methods. The structures of these states are reported.
Data exclusions	Following standard cryoEM data analysis procedures, many thousands of images were classified according to their quality. Images not having suitable quality or ice contamination were excluded.
Replication	Sample preparation for Cryo-EM analysis was repeated at least three times in independent experiments.
Randomization	Images of single particles were processed in two different mainstream software packages. In both cases single particle images were classified in canonical reference-free manner to exclude bias.
Blinding	There was no blinding. Particle images were picked and classified following standard cryoEM pipelines.

Reporting for specific materials, systems and methods

We require information from authors about some types of materials, experimental systems and methods used in many studies. Here, indicate whether each material, system or method listed is relevant to your study. If you are not sure if a list item applies to your research, read the appropriate section before selecting a response.

Materials & experimental systems

n/a	Involved in the study
☒	☐ Antibodies
☐	☒ Eukaryotic cell lines
☒	☐ Palaeontology and archaeology
☒	☐ Animals and other organisms
☒	☐ Clinical data
☒	☐ Dual use research of concern

Methods

n/a	Involved in the study
☒	☐ ChIP-seq
☒	☐ Flow cytometry
☒	☐ MRI-based neuroimaging

Eukaryotic cell lines

Policy information about cell lines and Sex and Gender in Research

Cell line source(s)	HEK293S GnTI- (#CRL-3022, ATCC) , SF9 (# 94-001F, Expression Systems).
Authentication	Vendor authentication.
Mycoplasma contamination	negative
Commonly misidentified lines (See ICLAC register)	Used cell lines are not on the ICLAC register.